sustainability

MDPI

Article

Simulation-Assisted Design Process of a 22 kW Wireless Power Transfer System Using Three-Phase Coil Coupling for EVs

Chia-Hsuan Wu [1], Ching-Ming Lai [1,*], Tomokazu Mishima [2] and Zheng-Bo Liang [1]

[1] Department of Electrical Engineering, National Chung Hsing University, Taichung 402, Taiwan; swdemperor@hotmail.com (C.-H.W.); brother87621@gmail.com (Z.-B.L.)
[2] Department of Marine Technologies and Engineerings, Faculty of Oceanology, Kobe University, Kobe 12885, Japan; mishima@maritime.kobe-u.ac.jp
* Correspondence: pecmlai@gmail.com

Abstract: The objective of this paper is to study a 22 kW high-power wireless power transfer (WPT) system for battery charging in electric vehicles (EVs). The proposed WPT system consists of a three-phase half-bridge LC–LC (i.e., primary LC/secondary LC) resonant power converter and a three-phase sandwich wound coil set (transmitter, Tx; receiver, Rx). To transfer power effectively with a 250 mm air gap, the WPT system uses three-phase, sandwich-wound Tx/Rx coils to minimize the magnetic flux leakage effect and increase the power transfer efficiency (PTE). Furthermore, the relationship of the coupling coefficient between the Tx/Rx coils is complicated, as the coupling coefficient is not only dominated by the coupling strength of the primary and secondary sides but also relates to the primary or secondary three-phase magnetic coupling effects. In order to analyze the proposed three-phase WPT system, a detailed equivalent circuit model is derived for a better understanding. To give a design reference, a novel coil design method that can achieve high conversion efficiency for a high-power WPT system was developed based on a simulation-assisted design procedure. A pair of magnetically coupled Tx and Rx coils and the circuit parameters of the three-phase half-bridge LC–LC resonant converter for a 22 kW WPT system are adjusted through PSIM and CST STUDIO SUITE™ simulation to execute the derivation of the design formulas. Finally, the system achieved a PTE of 93.47% at an 85 kHz operating frequency with a 170 mm air gap between the coils. The results verify the feasibility of a simulation-assisted design in which the developed coils can comply with a high-power and high-efficiency WPT system in addition to a size reduction.

Keywords: 22 kW wireless power transfer (WPT) system; three-phase (LC) (LC) resonant converter; sandwich coil coupling; circuit model; CST STUDIO SUITE™; PSIM

check for updates

Citation: Wu, C.-H.; Lai, C.-M.; Mishima, T.; Liang, Z.-B. Simulation-Assisted Design Process of a 22 kW Wireless Power Transfer System Using Three-Phase Coil Coupling for EVs. *Sustainability* **2021**, *13*, 12257. https://doi.org/10.3390/su132112257

Academic Editors: Nicu Bizon and Marc A. Rosen

Received: 12 August 2021
Accepted: 26 October 2021
Published: 6 November 2021

Publisher's Note: MDPI stays neutral with regard to jurisdictional claims in published maps and institutional affiliations.

Copyright: © 2021 by the authors. Licensee MDPI, Basel, Switzerland. This article is an open access article distributed under the terms and conditions of the Creative Commons Attribution (CC BY) license (https://creativecommons.org/licenses/by/4.0/).

1. Introduction

Electric vehicles (EVs) have the potential to serve as a solution to reducing petroleum consumption and as an alternative for replacing conventional fuel vehicles globally [1,2]. Major vehicle manufacturers are developing pure battery EVs, hybrid EVs (HEVs), and plug-in hybrid EVs (PHEVs) as their next-generation products [3,4]. Although EVs can help reduce global oil and gas depletion and environmental issues, the technology gap remains. EVs have limited mileage and battery capacity, longer charging periods, and higher overall costs. They also require charging cables, galvanic isolation components, battery chargers, and battery safety qualifications [5]. Furthermore, humidity, metallic particles, and air exposure can cause oxidation or rust on the charging gun for EVs due to long-term usage. Rust may cause overheating and potential fire risks when executing high-current transmissions during EV battery charging. Additionally, as the demand for higher battery capacity continues to grow, so does the size of the charging guns.

Generally, wireless charging, inductive power, non-contact charging, and contactless charging refer to the same technology [6–16]. Wireless charging is the technology of

electrically charging battery-powered devices without the need for a wired electrical connection. When compared to charging by wire, the WPT system is safe, efficient, and can reduce the loss of power transfer elements by preventing aging and oxidation by means of enhancing equipment durability [10]. Currently, three-phase topologies are considered to be most suitable for high-power WPT applications [8,9,13–16]. In the literature presented above, we do not see a complete and clarified design process for constructing cost-effective three-phase Tx/Rx coils due to the more complicated relationship of the coupling coefficient between the Tx/Rx coils.

Figure 1 is a schematic diagram of a WPT system for battery charging in an EV; it consists of an inverter, TX and RX coils, a rectifier, and a battery. The installation of a WPT system in EVs poses specific challenges, including limited storage space, restricted size of the coils, a potential decrease in efficiency, issues of misalignment tolerance, and increased overall costs.

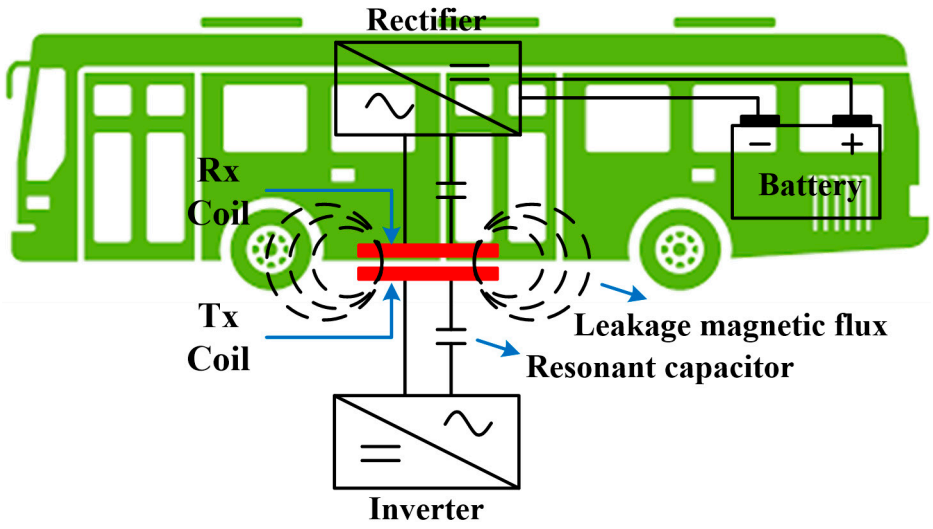


Figure 1. Schematic diagram of a WPT system for battery charging in an EV.

This paper developed a 22 kW high-power WPT system with a three-phase, half-bridge LC–LC resonant power converter and three-phase WPT sandwich-wound coils. The system operates at around a frequency of 85 kHz and complies with the SAE J2954 Z3 grade [17], based on inductive power transfer technology with magnetic resonance. Furthermore, in this paper, we proposed a novel coil design method to attain high conversion efficiency; PSIM and CST STUDIO SUITE™ simulation processes were used to design and adjust the parameters of the pair of magnetically coupled coils for the 22 kW WPT system, and then the design formulas were derived. Finally, the system achieved a PTE of 93.47% at a frequency of 85 kHz and with a 170 mm air gap between the Tx/Rx coils. The results indicate the effectiveness of the developed coil design method. The complete procedures for a high-power WPT system with high-efficiency and reduced coil size, which can demonstrate an overall performance that complies with the simulation-assisted design, were validated.

2. Circuit Topology

Figure 2 shows the circuit topology of the proposed three-phase high-power WPT system, which consists of an inverter with power MOSFETs (Q_1~Q_6), Tx/Rx coils with inductances (L_{1a}/L_{2a}, L_{1b}/L_{2b}, L_{1c}/L_{2c}), primary/secondary capacitors (C_{1a}/C_{2a}, C_{1b}/C_{2b}, C_{1c}/C_{2c}), the output rectifier with power diodes (D_1~D_6), the output filter capacitor (C_o), and load resistance (R_L).

In Figure 2, the circuit topology consists of three half-bridge LC–LC resonant power modules connected in parallel. Note that the phase difference of the control signals is 120° for each power module.

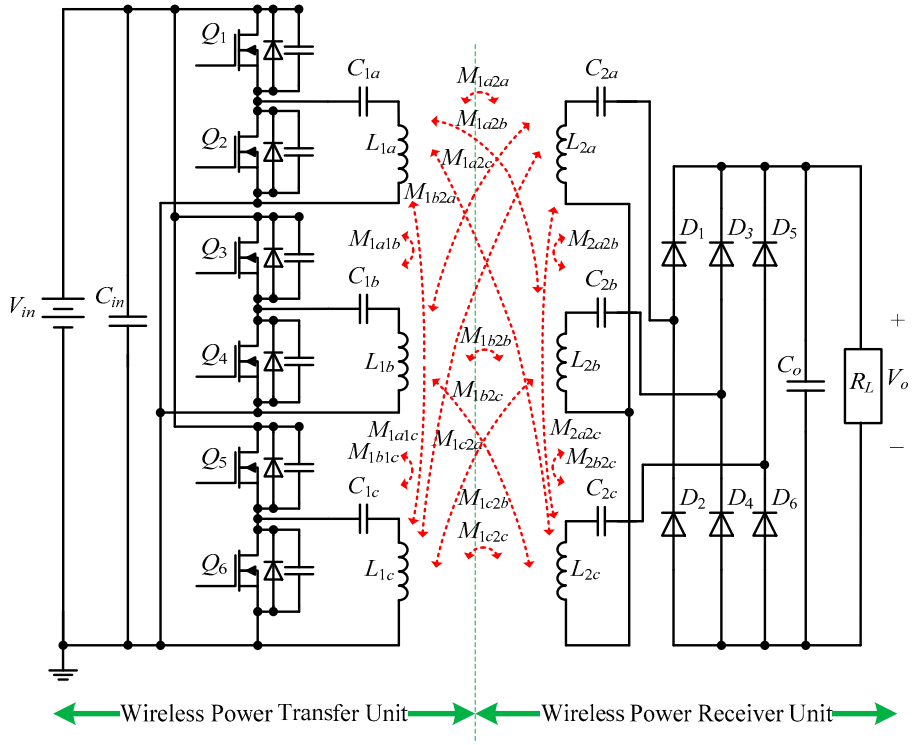


Figure 2. Proposed circuit topology for the three-phase high-power WPT system.

A novel sandwich-wound overlapping structure design is adopted in this paper to reduce the size of the three-phase Tx/Rx coils, which improves the power density of the WPT system. However, the relationship of the coupling coefficient between the three-phase Tx/Rx coils is more complicated, as the coupling coefficient is dominated by the coupling strength of the primary and secondary sides and relates to the primary or secondary three-phase magnetic coupling effects. To obtain a better understanding of the three-phase coil design concept, an equivalent circuit model is derived by reflecting the secondary side impedance to the primary side to analyze the proposed three-phase circuit topology. The circuit parameters are derived based on the specifications shown in Table 1 and were followed by simulations to verify the proposed feasibility.

Table 1. Specifications of the 22 kW WPT system.

Inverter input voltage (V_{in})	750 V
Rectifier output voltage (V_o)	450 V
Output power (P_o)	22 kW
Operating frequency	85 kHz
Transmission distance (air gap)	170 mm~250 mm

As shown in Figure 3, the load resistance (R_o) is reflected into the equivalent resistance (R_{La}, R_{Lb}, R_{Lc}) of the corresponding three-phase coils. Assuming that the three-phase coils are balanced and the rectifier circuit has no power loss, one can obtain the following equation [18]:

$$R_{La} = R_{Lb} = R_{Lc} = \frac{6}{\pi^2} R_L \quad (1)$$

The parameters of the secondary side circuit can be reflected to the primary side to simplify the analysis; thus, the circuit in Figure 4a is equivalent to the single loop circuit shown in Figure 4b.

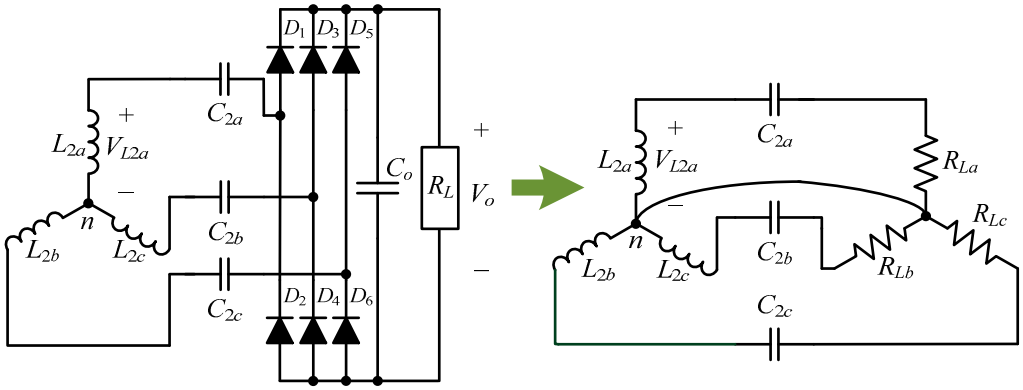


Figure 3. Equivalent circuit by reflecting a secondary side impedance to the primary side.

In Figure 4a, the primary side voltages (V_{L1a}, V_{L1b}, V_{L1c}) and the secondary side voltages (V_{L2a}, V_{L2b}, V_{L2c}) of the three-phase coils can be obtained according to Kirchhoff's voltage law. The circuit equation relationship of the primary side can be expressed as Equation (2) and on the secondary side as Equation (3).

$$\begin{bmatrix} V_{L1a} \\ V_{L1b} \\ V_{L1c} \end{bmatrix} = \begin{bmatrix} V_{ina} \\ V_{inb} \\ V_{inc} \end{bmatrix} + \begin{bmatrix} -\frac{1}{sC_{1a}} & -sM_{1a1b} & -sM_{1a1c} \\ -sM_{1a1b} & -\frac{1}{sC_{1b}} & -sM_{1b1c} \\ -sM_{1a1c} & -sM_{1b1c} & -\frac{1}{sC_{1c}} \end{bmatrix} \begin{bmatrix} I_{1a} \\ I_{1b} \\ I_{1c} \end{bmatrix} \tag{2}$$

$$\begin{bmatrix} V_{L2a} \\ V_{L2b} \\ V_{L2c} \end{bmatrix} = \begin{bmatrix} -R_{La} - \frac{1}{sC_{1a}} & -sM_{2a2b} & -sM_{2a2c} \\ -sM_{2a2b} & -R_{Lb} - \frac{1}{sC_{1b}} & -sM_{2b2c} \\ -sM_{2a2c} & -sM_{2b2c} & -R_{Lc} - \frac{1}{sC_{1c}} \end{bmatrix} \begin{bmatrix} I_{2a} \\ I_{2b} \\ I_{2c} \end{bmatrix} \tag{3}$$

The primary side voltages (V_{L1a}, V_{L1b}, V_{L1c}) and the secondary side voltages (V_{L2a}, V_{L2b}, V_{L2c}) can also be obtained by considering the primary or secondary three-phase magnetic coupling effects as shown in Equations (4) and (5):

$$\begin{bmatrix} V_{L1a} \\ V_{L1b} \\ V_{L1c} \end{bmatrix} = \begin{bmatrix} sL_{1a}I_{1a} \\ sL_{1b}I_{1b} \\ sL_{1c}I_{1c} \end{bmatrix} + \begin{bmatrix} sM_{1a2a} & sM_{1a2b} & sM_{1a2c} \\ sM_{1b2a} & sM_{1b2b} & sM_{1b2c} \\ sM_{1c2a} & sM_{1c2b} & sM_{1c2c} \end{bmatrix} \begin{bmatrix} I_{2a} \\ I_{2b} \\ I_{2c} \end{bmatrix} \tag{4}$$

$$\begin{bmatrix} V_{L2a} \\ V_{L2b} \\ V_{L2c} \end{bmatrix} = \begin{bmatrix} sL_{2a}I_{2a} \\ sL_{2b}I_{2b} \\ sL_{2c}I_{2c} \end{bmatrix} + \begin{bmatrix} sM_{1a2a} & sM_{1b2a} & sM_{1c2a} \\ sM_{1a2b} & sM_{1b2b} & sM_{1c2b} \\ sM_{1a2c} & sM_{1b2c} & sM_{1c2c} \end{bmatrix} \begin{bmatrix} I_{1a} \\ I_{1b} \\ I_{1c} \end{bmatrix} \tag{5}$$

where Equation (2) is equal to Equation (4); Equation (3) is equal to Equation (5).

Rearranging Equations (4) and (5) leads to the following:

$$\begin{bmatrix} V_{ina} \\ V_{inb} \\ V_{inc} \end{bmatrix} + \begin{bmatrix} -\frac{1}{sC_{1a}} & -sM_{1a1b} & -sM_{1a1c} \\ -sM_{1a1b} & -\frac{1}{sC_{1b}} & -sM_{1b1c} \\ -sM_{1a1c} & -sM_{1b1c} & -\frac{1}{sC_{1c}} \end{bmatrix} \begin{bmatrix} I_{1a} \\ I_{1b} \\ I_{1c} \end{bmatrix} = \begin{bmatrix} sL_{1a}I_{1a} \\ sL_{1b}I_{1b} \\ sL_{1c}I_{1c} \end{bmatrix} + \begin{bmatrix} sM_{1a2a} & sM_{1a2b} & sM_{1a2c} \\ sM_{1b2a} & sM_{1b2b} & sM_{1b2c} \\ sM_{1c2a} & sM_{1c2b} & sM_{1c2c} \end{bmatrix} \begin{bmatrix} I_{2a} \\ I_{2b} \\ I_{2c} \end{bmatrix} \tag{6}$$

$$\begin{bmatrix} sL_{2a}I_{2a} \\ sL_{2b}I_{2b} \\ sL_{2c}I_{2c} \end{bmatrix} + \begin{bmatrix} sM_{1a2a} & sM_{1b2a} & sM_{1c2a} \\ sM_{1a2b} & sM_{1b2b} & sM_{1c2b} \\ sM_{1a2c} & sM_{1b2c} & sM_{1c2c} \end{bmatrix} \begin{bmatrix} I_{1a} \\ I_{1b} \\ I_{1c} \end{bmatrix} = \begin{bmatrix} -R_{La} - \frac{1}{sC_{2a}} & -sM_{2a2b} & -sM_{2a2c} \\ -sM_{2a2b} & -R_{Lb} - \frac{1}{sC_{2b}} & -sM_{2b2c} \\ -sM_{2a2c} & -sM_{2b2c} & -R_{Lc} - \frac{1}{sC_{2c}} \end{bmatrix} \begin{bmatrix} I_{2a} \\ I_{2b} \\ I_{2c} \end{bmatrix} \tag{7}$$

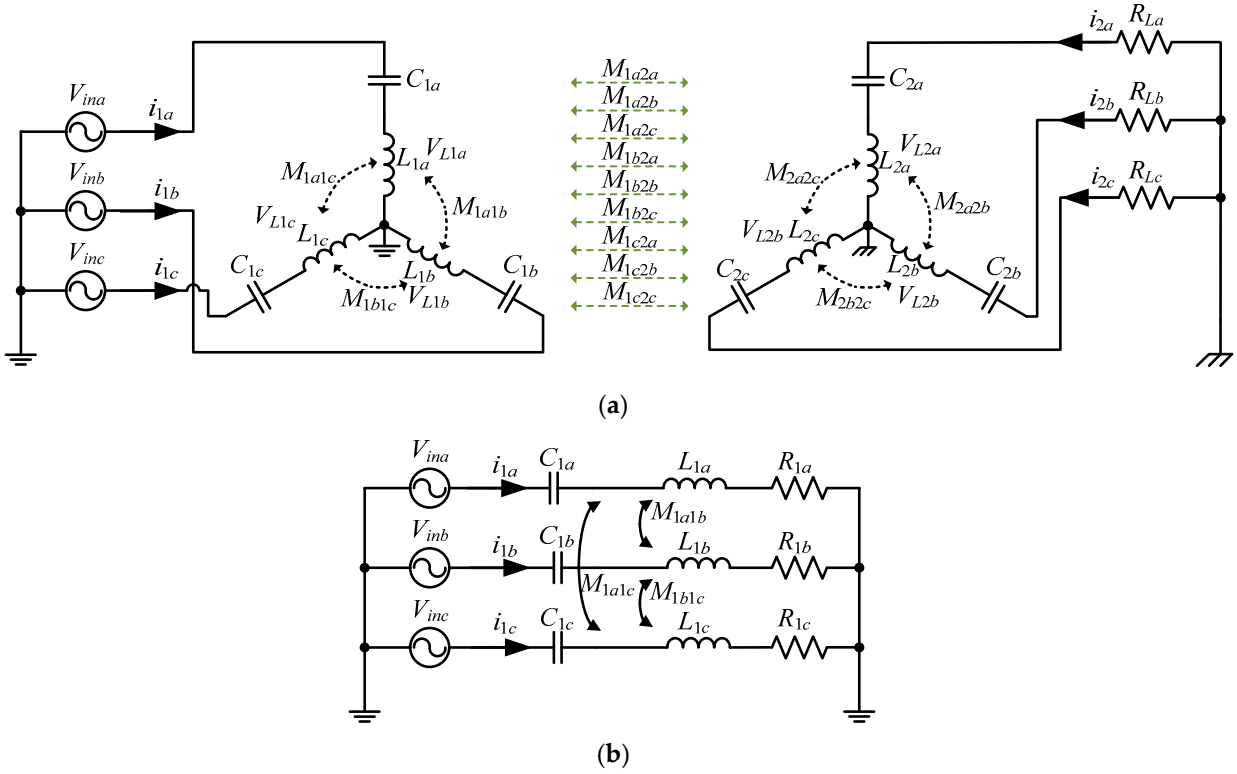


Figure 4. Three-phase coil coupling: (**a**) topology; (**b**) equivalent circuit.

From Equation (6), if one eliminates the coupling factors caused by secondary side currents (I_{2a}, I_{2b}, I_{2c}), the relationship of the equivalent circuit from the secondary side mapped to the primary side can be derived accordingly. In Equation (7), one can see the relationship between the primary and secondary side currents. As the circuit is designed as a series resonant WPT, the secondary side coil inductors are resonated with the secondary side capacitors, which can be derived as Equations (8)–(10) [19]. It is notable that the parameters of the coil inductors are dominated by the coupling strength of the primary and secondary sides and relate to the primary or secondary three-phase magnetic coupling effects. The coil inductors should be selected with fine-tuning at first through the CST STUDIO SUITE™ simulation (referring to Section 3).

$$C_{2a} = \frac{1}{(L_{2a} - M_{2a2b} - M_{2a2c} + M_{2b2c})\omega^2} \tag{8}$$

$$C_{2b} = \frac{1}{(L_{2b} - M_{2a2b} - M_{2b2c} + M_{2a2c})\omega^2} \tag{9}$$

$$C_{2c} = \frac{1}{(L_{2c} - M_{2a2c} - M_{2b2c} + M_{2a2b})\omega^2} \tag{10}$$

Once the secondary-side resonant parameters are confirmed, substituting Equations (8)–(10) into Equation (6) yields the relationship between the primary side and secondary side currents, as seen below:

$$I_{2a} = \frac{s\alpha_{1a2a}I_{1a} + s\alpha_{1b2a}I_{1b} + s\alpha_{1c2a}I_{1c}}{R_{Labc}} \tag{11}$$

$$I_{2b} = \frac{s\alpha_{1a2b}I_{1a} + s\alpha_{1b2b}I_{1b} + s\alpha_{1c2b}I_{1c}}{R_{Labc}} \tag{12}$$

$$I_{2c} = \frac{s\alpha_{1a2c}I_{1a} + s\alpha_{1b2c}I_{1b} + s\alpha_{1c2c}I_{1c}}{R_{Labc}} \tag{13}$$

where

$$R_{Labc} = R_{La}R_{Lb} + R_{La}R_{Lc} + R_{Lb}R_{Lc} \tag{14}$$

$$\begin{Bmatrix} \alpha_{1a2a} = M_{1a2c}R_{Lb} + M_{1a2b}R_{Lc} - M_{1a2a}(R_{Lb} + R_{Lc}); \alpha_{1b2a} = M_{1b2c}R_{Lb} + M_{1b2b}R_{Lc} - M_{1b2a}(R_{Lb} + R_{Lc}); \\ \alpha_{1c2a} = M_{1c2c}R_{Lb} + M_{1c2b}R_{Lc} - M_{1c2a}(R_{Lb} + R_{Lc}) \end{Bmatrix}$$
$$\begin{Bmatrix} \alpha_{1a2b} = M_{1a2c}R_{La} + M_{1a2a}R_{Lc} - M_{1a2b}(R_{La} + R_{Lc}); \alpha_{1b2b} = M_{1b2c}R_{La} + M_{1b2a}R_{Lc} - M_{1b2b}(R_{La} + R_{Lc}); \\ \alpha_{1c2b} = M_{1c2c}R_{La} + M_{1c2a}R_{Lc} - M_{1c2b}(R_{La} + R_{Lc}) \end{Bmatrix} \tag{15}$$
$$\begin{Bmatrix} \alpha_{1a2c} = M_{1a2b}R_{La} + M_{1a2a}R_{Lb} - M_{1a2c}(R_{La} + R_{Lb}); \alpha_{1b2c} = M_{1b2b}R_{La} + M_{1b2a}R_{Lb} - M_{1b2c}(R_{La} + R_{Lb}); \\ \alpha_{1c2c} = M_{1c2b}R_{La} + M_{1c2a}R_{Lb} - M_{1c2c}(R_{La} + R_{Lb}) \end{Bmatrix}$$

Once the relationship between the primary and secondary side currents is obtained, Equations (11)–(13) can be substituted into (6) to calculate the circuit parameters. Then, Equation (7) is arranged to obtain (16):

$$\begin{bmatrix} V_{ina} \\ V_{inb} \\ V_{inc} \end{bmatrix} = \begin{bmatrix} sL_{1a} + \frac{1}{sC_{1a}} & sM_{1a1b} & sM_{1a1c} \\ sM_{1a1b} & sL_{1b} + \frac{1}{sC_{1b}} & sM_{1b1c} \\ sM_{1a1c} & sM_{1b1c} & sL_{1c} + \frac{1}{sC_{1c}} \end{bmatrix} \begin{bmatrix} I_{1a} \\ I_{1b} \\ I_{1c} \end{bmatrix} + \begin{bmatrix} \frac{s^2\beta_{1a1a}}{R_{Labc}} & \frac{s^2\beta_{1a1b}}{R_{Labc}} & \frac{s^2\beta_{1a1c}}{R_{Labc}} \\ \frac{s^2\beta_{1b1a}}{R_{Labc}} & \frac{s^2\beta_{1b1b}}{R_{Labc}} & \frac{s^2\beta_{1b1c}}{R_{Labc}} \\ \frac{s^2\beta_{1c1a}}{R_{Labc}} & \frac{s^2\beta_{1c1b}}{R_{Labc}} & \frac{s^2\beta_{1c1c}}{R_{Labc}} \end{bmatrix} \begin{bmatrix} I_{1a} \\ I_{1b} \\ I_{1c} \end{bmatrix} \tag{16}$$

where

$$\begin{Bmatrix} \beta_{1a1a} = M_{1a2a}\alpha_{1a2a} + M_{1a2b}\alpha_{1a2b} - M_{1a2c}\alpha_{1a2c}; \beta_{1a1b} = M_{1a2a}\alpha_{1b2a} + M_{1a2b}\alpha_{1b2b} - M_{1a2c}\alpha_{1b2c} \\ \beta_{1a1c} = M_{1a2a}\alpha_{1c2a} + M_{1a2b}\alpha_{1c2b} - M_{1a2c}\alpha_{1c2c} \end{Bmatrix}$$
$$\begin{Bmatrix} \beta_{1b1a} = M_{1b2a}\alpha_{1a2a} + M_{1b2b}\alpha_{1a2b} - M_{1b2c}\alpha_{1a2c}; \beta_{1b1b} = M_{1b2a}\alpha_{1b2a} + M_{1b2b}\alpha_{1b2b} - M_{1b2c}\alpha_{1b2c} \\ \beta_{1b1c} = M_{1b2a}\alpha_{1c2a} + M_{1b2b}\alpha_{1c2b} - M_{1b2c}\alpha_{1c2c} \end{Bmatrix} \tag{17}$$
$$\begin{Bmatrix} \beta_{1c1a} = M_{1c2a}\alpha_{1a2a} + M_{1c2b}\alpha_{1a2b} - M_{1c2c}\alpha_{1a2c}; \beta_{1c1b} = M_{1c2a}\alpha_{1b2a} + M_{1c2b}\alpha_{1b2b} - M_{1c2c}\alpha_{1b2c} \\ \beta_{1c1c} = M_{1c2a}\alpha_{1c2a} + M_{1c2b}\alpha_{1c2b} - M_{1c2c}\alpha_{1c2c} \end{Bmatrix}$$

Similarly, the primary side resonant capacitors can be derived with Equation (16), as seen below:

$$C_{1a} = \frac{1}{(L_{1a} - M_{1a1b} - M_{1a1c} + M_{1b1c})\omega^2} \tag{18}$$

$$C_{1b} = \frac{1}{(L_{1b} - M_{1a1b} - M_{1b1c} + M_{1a1c})\omega^2} \tag{19}$$

$$C_{1c} = \frac{1}{(L_{1c} - M_{1a1c} - M_{1b1c} + M_{1a1b})\omega^2} \tag{20}$$

Once the primary side resonant capacitances are obtained, the capacitance parameters Equations (18)–(20) can be substituted into Equation (16) and derived as

$$\begin{bmatrix} V_{ina} \\ V_{inb} \\ V_{inc} \end{bmatrix} = \begin{bmatrix} -sM_{1b1c} & -sM_{1a1c} & -sM_{1a1b} \\ -sM_{1b1c} & -sM_{1a1c} & -sM_{1a1b} \\ -sM_{1b1c} & -sM_{1a1c} & -sM_{1a1b} \end{bmatrix} \begin{bmatrix} I_{1a} \\ I_{1b} \\ I_{1c} \end{bmatrix} + \begin{bmatrix} \frac{s^2\beta_{1a1a}}{R_{Labc}} & \frac{s^2\beta_{1a1b}}{R_{Labc}} & \frac{s^2\beta_{1a1c}}{R_{Labc}} \\ \frac{s^2\beta_{1b1a}}{R_{Labc}} & \frac{s^2\beta_{1b1b}}{R_{Labc}} & \frac{s^2\beta_{1b1c}}{R_{Labc}} \\ \frac{s^2\beta_{1c1a}}{R_{Labc}} & \frac{s^2\beta_{1c1b}}{R_{Labc}} & \frac{s^2\beta_{1c1c}}{R_{Labc}} \end{bmatrix} \begin{bmatrix} I_{1a} \\ I_{1b} \\ I_{1c} \end{bmatrix} \tag{21}$$

Referring to Figure 4b and Equation (21), to calculate the resistances (R_{1a}, R_{1b}, R_{1c}) of the equivalent circuit, the source voltage (V_{inb}) is subtracted from the source voltage (V_{ina}), the source voltage (V_{inc}) is subtracted from the source voltage (V_{inb}), and the source voltage (V_{ina}) is subtracted from the source voltage (V_{inc}), summarized below:

$$V_{ina} - V_{inb} = I_{1a}\frac{s^2}{R_{Labc}}(\beta_{1a1a} - \beta_{1a1c} - \beta_{1b1a} + \beta_{1b1c}) - I_{1b}\frac{s^2}{R_{Labc}}(\beta_{1b1b} - \beta_{1b1c} - \beta_{1a1b} + \beta_{1a1c}) \tag{22}$$

$$V_{inb} - V_{inc} = I_{1b}\frac{s^2}{R_{Labc}}(\beta_{1b1b} - \beta_{1b1a} - \beta_{1c1b} + \beta_{1c1a}) - I_{1c}\frac{s^2}{R_{Labc}}(\beta_{1c1c} - \beta_{1c1a} - \beta_{1b1c} + \beta_{1b1a}) \tag{23}$$

$$V_{inc} - V_{ina} = I_{1c}\frac{s^2}{R_{Labc}}(\beta_{1c1c} - \beta_{1c1b} - \beta_{1a1c} + \beta_{1a1b}) - I_{1a}\frac{s^2}{R_{Labc}}(\beta_{1a1a} - \beta_{1a1b} - \beta_{1c1a} + \beta_{1c1b}) \tag{24}$$

From Equations (22)–(24), the equivalent resistance in Equations (25)–(27) can be derived as seen below:

$$R_{1a} = \frac{-\omega^2}{R_{Labc}}(\beta_{1a1a} - \beta_{1a1c} - \beta_{1b1a} + \beta_{1b1c}) = \frac{-\omega^2}{R_{Labc}}(\beta_{1a1a} - \beta_{1a1b} - \beta_{1c1a} + \beta_{1c1b}) \quad (25)$$

$$R_{1b} = \frac{-\omega^2}{R_{Labc}}(\beta_{1b1b} - \beta_{1b1c} - \beta_{1a1b} + \beta_{1a1c}) = \frac{-\omega^2}{R_{Labc}}(\beta_{1b1b} - \beta_{1b1a} - \beta_{1c1b} + \beta_{1c1a}) \quad (26)$$

$$R_{1c} = \frac{-\omega^2}{R_{Labc}}(\beta_{1c1c} - \beta_{1c1a} - \beta_{1b1c} + \beta_{1b1a}) = \frac{-\omega^2}{R_{Labc}}(\beta_{1c1c} - \beta_{1c1b} - \beta_{1a1c} + \beta_{1a1b}) \quad (27)$$

Once the equivalent resistance reflected to the primary side is obtained, Figure 2 is equivalent to the circuit diagram, as seen in Figure 5. The output power to the primary side coil of the inverter module can be expressed as Equations (28)–(31):

$$P_{1a} = \frac{2}{\pi^2}\frac{V_{in}^2}{R_{1a}} = \frac{2}{\pi^2}\frac{V_{in}^2}{\frac{-\omega^2}{R_{Labc}}(\beta_{1a1a} - \beta_{1a1c} - \beta_{1b1a} + \beta_{1b1c})} \quad (28)$$

$$P_{1b} = \frac{2}{\pi^2}\frac{V_{in}^2}{R_{1b}} = \frac{2}{\pi^2}\frac{V_{in}^2}{\frac{-\omega^2}{R_{Labc}}(\beta_{1b1b} - \beta_{1b1c} - \beta_{1a1b} + \beta_{1a1c})} \quad (29)$$

$$P_{1c} = \frac{2}{\pi^2}\frac{V_{in}^2}{R_{1c}} = \frac{2}{\pi^2}\frac{V_{in}^2}{\frac{-\omega^2}{R_{Labc}}(\beta_{1c1c} - \beta_{1c1a} - \beta_{1b1c} + \beta_{1b1a})} \quad (30)$$

$$P_t = \frac{6}{\pi^2}\frac{V_{in}^2}{\frac{-\omega^2}{1.11R_L^2}(\beta_{1a1a} - \beta_{1a1c} - \beta_{1b1a} + \beta_{1b1c})} \quad (31)$$

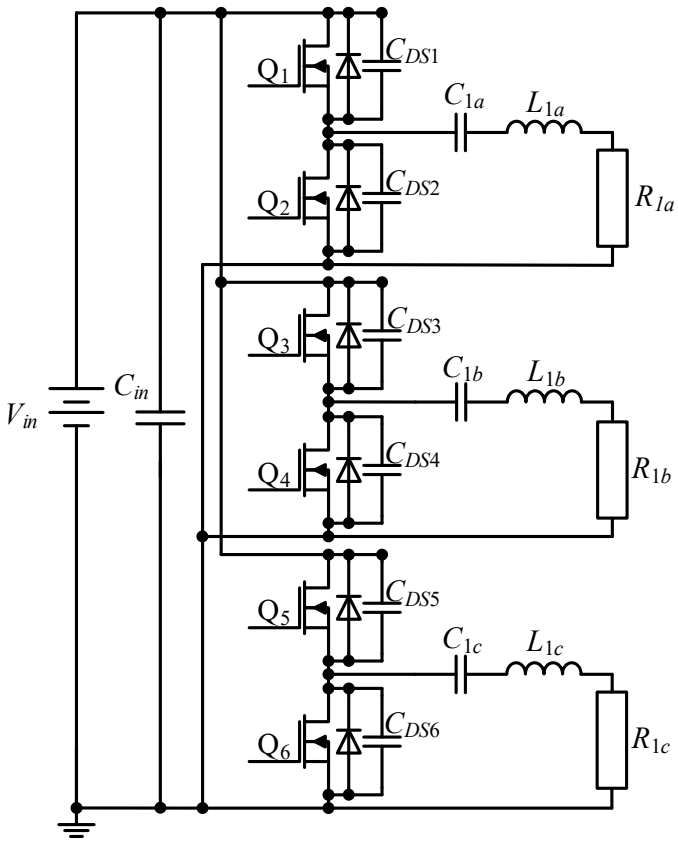


Figure 5. Three-phase coil coupling equivalent circuit on the primary side.

In summary, all the equations are discussed in the previous description; once the required power, output voltage, coil parameters, and operating frequency are confirmed, the parameters of the circuit can be calculated by Equations (18)–(20) and (31).

3. Coil Design

The coil design was processed in advance using PSIM and CST STUDIO SUITE™ for self-inductance (i.e., coil inductor), coupling coefficient, misalignment effects, and voltage gain for the WPT converter design in order to reach the specifications shown in Table 1 with higher efficiency. Figure 6 shows the proposed sandwich wound coils, which overlap at an angle difference of 120°; it provides the following features: (i) compact size to provide good reliability and light weight; and (ii) a high coupling coefficient and better tolerance of misalignment between primary and secondary coils to enhance efficiency and keep the variation in parameters small for reasonable control.

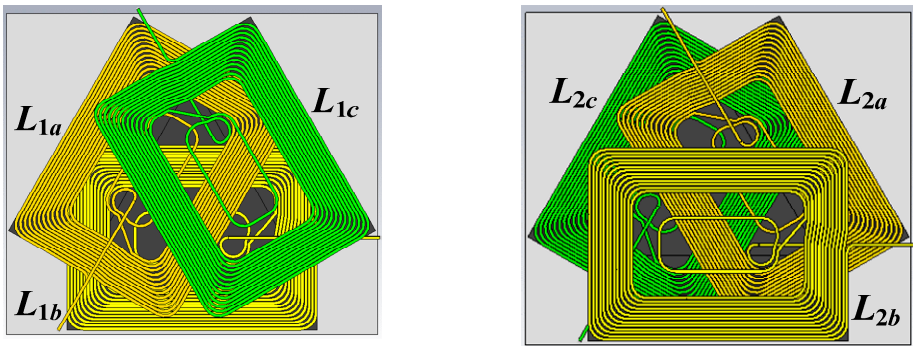


Figure 6. Proposed three-phase coil structure and drawing: (**a**) Tx coils; (**b**) Rx coils.

In Figure 6, the Tx coils and Rx coils are equal in design size; the corresponding design specifications are shown in Table 2. The main difference is that the overlapping order is different from the arrangement of the magnetic materials.

Table 2. Coil specifications and design parameters.

Coil Type	Tx/Rx Coils
Size	600 mm × 450 mm
Number of turns	14
Wire thickness	8 mm
Magnetic material specification	
Magnetic material	Ferrite FAT100 xiaoshuang(Crown Ferrite Enterprise Co.)
Magnetic material size	882 m × 763 mm
Magnetic material thickness	5 mm
Magnetic field shielding plates	
Shielding plate material	Aluminum
Shielding plate size	890 mm × 780 mm
Shielding plate thickness	6 mm

To make the three sets of coils approach balance in design, the sub-coils on the primary and secondary side coupling have the same coupling distance; hence, the lowermost coil of the primary side corresponds to the uppermost coil of the secondary side and the uppermost coil of the primary side corresponds to the lowermost coil of the secondary side. Furthermore, the arrangements of the Tx and Rx coils are different; as a result, L_{1a} corresponds to L_{2a}, L_{1b} corresponds to L_{2b}, and L_{1c} corresponds to L_{2c}. To avoid imbalance of the inductance of the Tx/Rx coils, one arranges the magnetic material at different heights

instead of placing it under the coils, as shown in Figure 7. Thus, the coils can achieve similar inductance, as verified by simulations.



Figure 7. Magnetic material placement.

Based on the coil drawing schematic shown in Figures 6 and 7, the simulation results using CST STUDIO SUITE™ are listed in Table 3. It can be seen that the simulated results for the inductance of the Tx and Rx coils approach the balance condition.

Table 3. CST STUDIO SUITE™ simulation results of the Tx and Rx coils.

Items	Tx Coils			Rx Coils		
Self-inductance (μH)	L_{1a} 131	L_{1b} 131.1	L_{1c} 130.3	L_{2a} 130.9	L_{2b} 130.6	L_{2c} 130.7
Mutual inductance (μH)	M_{1b1a} 33.26	M_{1c1b} 33.69	M_{1a1c} 35.6	M_{1b1a} 35.67	M_{1c1b} 33.64	M_{1a1c} 33.07

Figure 8 shows the 3D Tx/Rx coupling schematic diagram with CST STUDIO SUITE™, where L_{1a} corresponds to L_{2a}, L_{1b} corresponds to L_{2b}, and L_{1c} corresponds to L_{2c}. According to the SAE J2954 Z3 grade [17], the air gap and power transmission distance between the Rx and Tx coil coupling are 170 mm to 250 mm. Figure 9 shows the mutual inductance values under different air gap distances for the primary and secondary side coil coupling. In Figure 9, M_{1a2a} is the mutual inductance of coils L_{1a} and L_{2a}, which has a positive alignment relationship and is larger than M_{1a2b} (i.e., the mutual inductance of coils L_{1a} and L_{2b}) and M_{1a2c} (i.e., the mutual inductance of coils L_{1a} and L_{2c}). When misalignment occurs, the conversion efficiency will decrease due to the reduction in the coils' magnetic coupling.

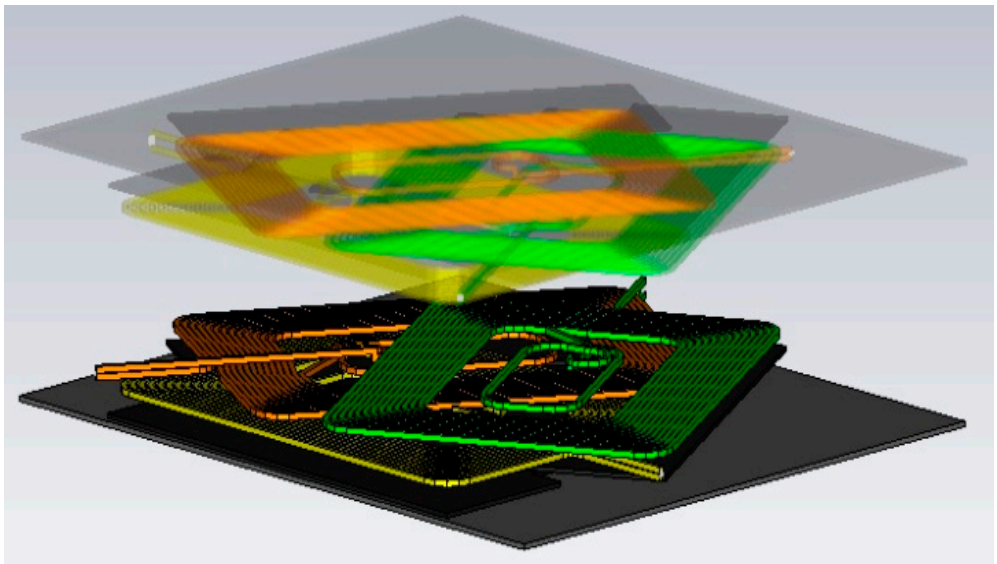


Figure 8. 3D Tx/Rx coupling schematic diagram with CST STUDIO SUITE™.

Similarly, M_{1b2b} of coils L_{1b} and L_{2b} is larger than M_{1a2b} (i.e., the mutual inductance of coils L_{1a} and L_{2b}) and M_{1c2b} (i.e., the mutual inductance of coils L_{1c} and L_{2b}). Once the

self-inductance and mutual inductance parameters of the Tx/Rx coils are selected, these are substituted into Equations (18)–(20) and (31) to calculate the resonant capacitors (referring to Section 2).

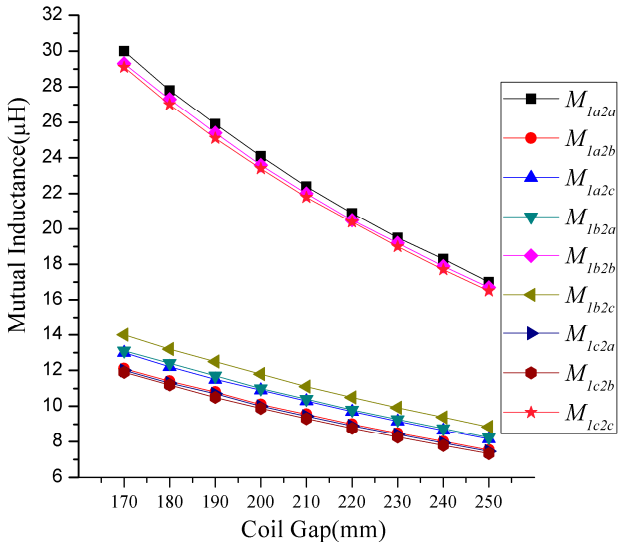


Figure 9. Simulated results of mutual inductance under different air gap distances.

4. Results

To validate the derived equation of the proposed WPT system, the circuit schematic was drawn with PSIM software as shown in Figure 10; the calculated parameters are listed in Table 4.

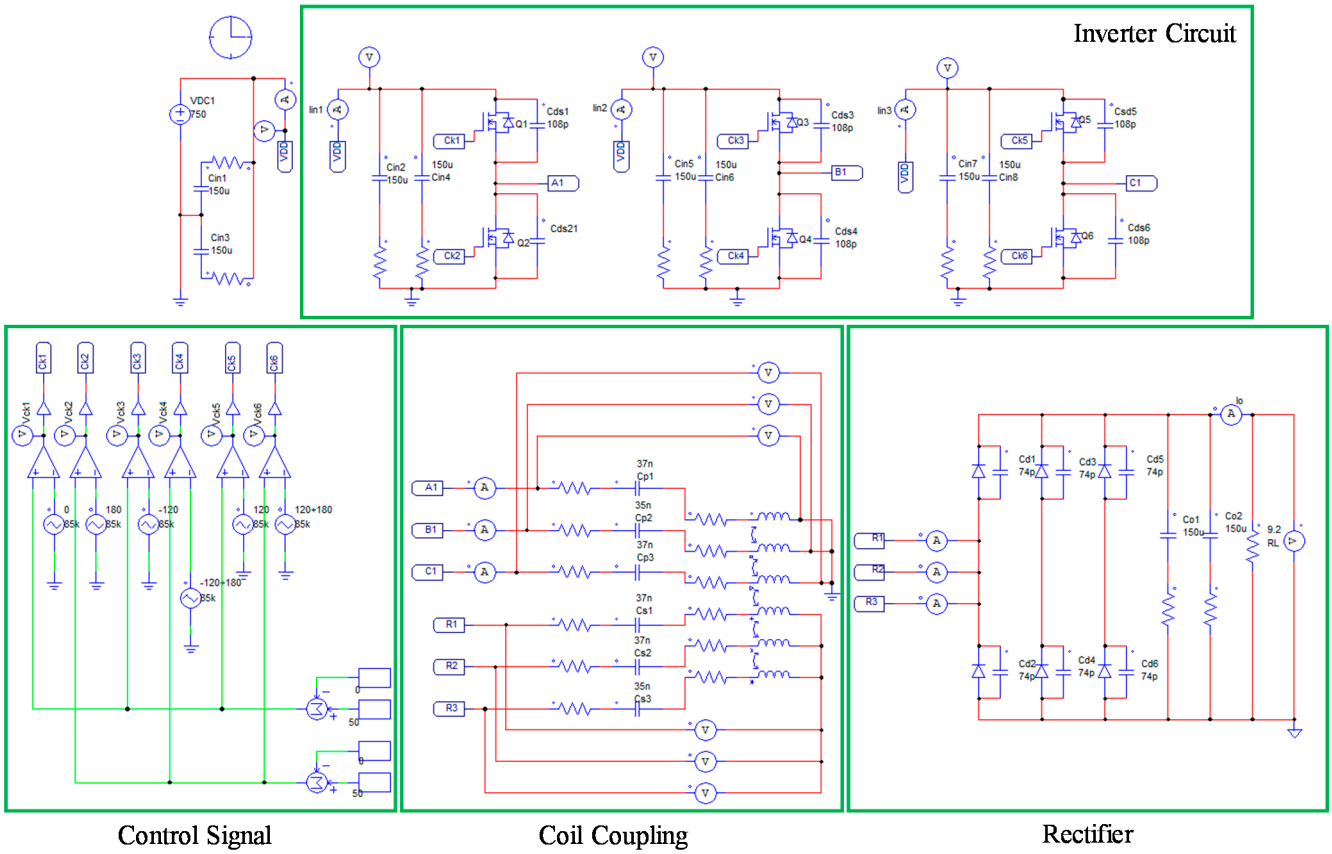


Figure 10. PSIM circuit simulation schematic of the proposed 22 kW WPT system.

Table 4. PSIM circuit simulation parameters of the proposed 22 kW WPT system.

Primary coils (μH)	L_{1a}	L_{1b}	L_{1c}	M_{1b1a}	M_{1c1b}	M_{1a1c}
	131	131.1	130.3	33.26	33.69	35.6
Secondary coils (μH)	L_{2a}	L_{2b}	L_{2c}	M_{2b2a}	M_{2c2b}	M_{2a2c}
	130.9	130.6	130.7	35.67	33.64	33.07
Output resistor R_L	Simulation (9.2 Ω)			Calculation (9 Ω)		
Mutual inductance (μH)	M_{1a2a}		M_{1b2a}		M_{1c2a}	
	29.96		13.13		12.02	
Primary side capacitors (nF)	Simulation			Calculation		
	C_{1a}	C_{1b}	C_{1c}	C_{1a}	C_{1b}	C_{1c}
	36.6	35.2	37.2	39	34.5	36.5
Secondary side capacitors (nF)	Simulation			Calculation		
	C_{1a}	C_{1b}	C_{1c}	C_{1a}	C_{1b}	C_{1c}
	36.6	37.2	35.2	37	37	35

In Figure 10, a half-bridge leg is used as the inverter module, and a three-phase diode circuit is used as the secondary-side rectifier. Furthermore, the coil coupling circuit includes three-phase, sandwich-wound Tx/Rx coils; the series resonant capacitors; and the reflected load resistances. To control the inverter module, as shown in Figure 11, one sets the pulse-width modulation (PWM) signal at 50% duty cycle and 85 kHz. The phase difference between the upper power switch and lower power switch of the inverter module is 180°; the phase difference of the three inverter modules is 120°.

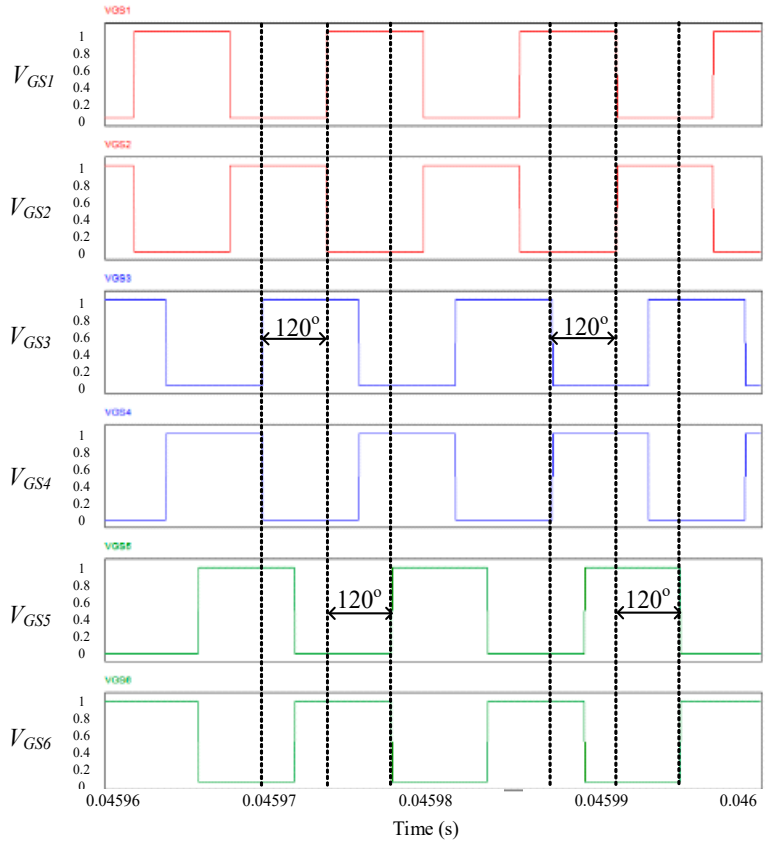


Figure 11. Control signals of the inverter.

The simulated and calculated circuit parameters are summarized and listed in Table 4. One can see that the primary side capacitances are slightly different from the calculation results because of the parasitic capacitance effect of the power switch of the inverter module. Therefore, the primary side capacitances need to be modified slightly to make the power switch operate with zero voltage switching (ZVS). Figure 12 shows the ZVS waveforms of the power switch for the inverter; the drain voltages and conducting currents of the three half-bridge power modules are measured, respectively. From Figure 12, it can be seen that the switch current is nearly zero when the switch is turned on, which shows that the ZVS condition in this instant is provided, and the efficiency can be improved.

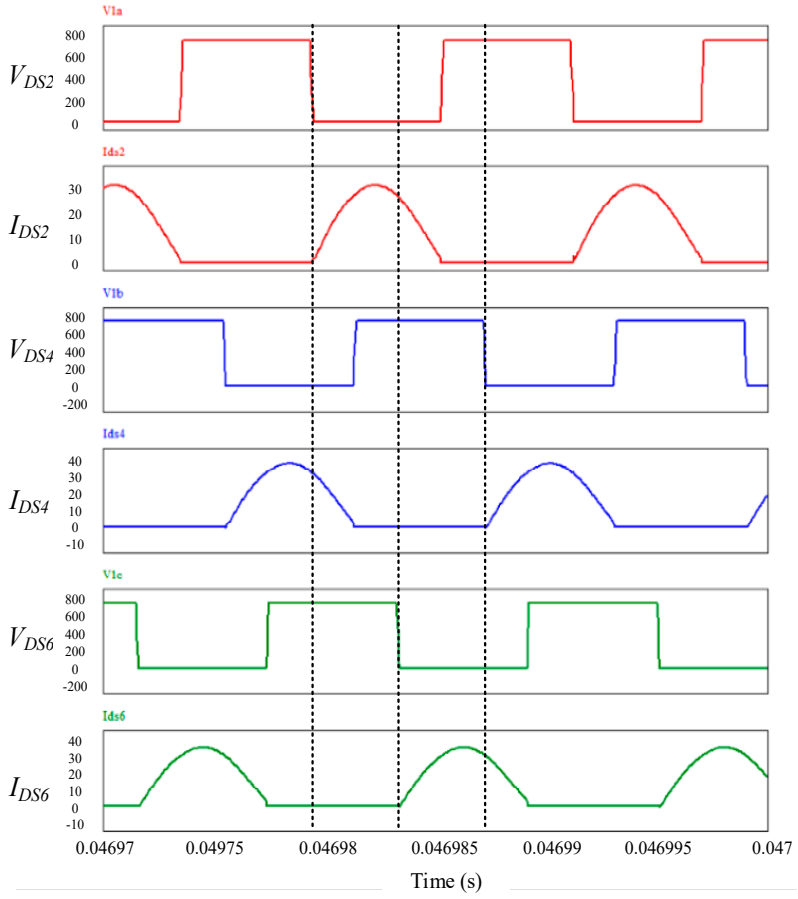


Figure 12. ZVS waveforms of the inverter.

Figure 13 shows the waveforms of the input voltage (V_{in}) and the output voltage (V_o); when the input voltage is about 750 V, the WPT system can regulate the output voltage to 449.75 V, close to the specification voltage shown in Table 1. Figure 14 shows the conversion efficiency of the WPT system with a 170 mm air gap; it indicates that the input power is 24.05 kW, the output power is 22.48 kW, and the efficiency is 93.47%, thus achieving a high-efficiency WPT design. Based on the simulation-assisted design results of Figure 6, the realized prototype of the Tx/Rx coils was built, as shown in Figures 15 and 16. The measured results of the coil prototypes are also listed in Table 5; the tolerances of parameters are limited to 7~18%, compared with the designed points.

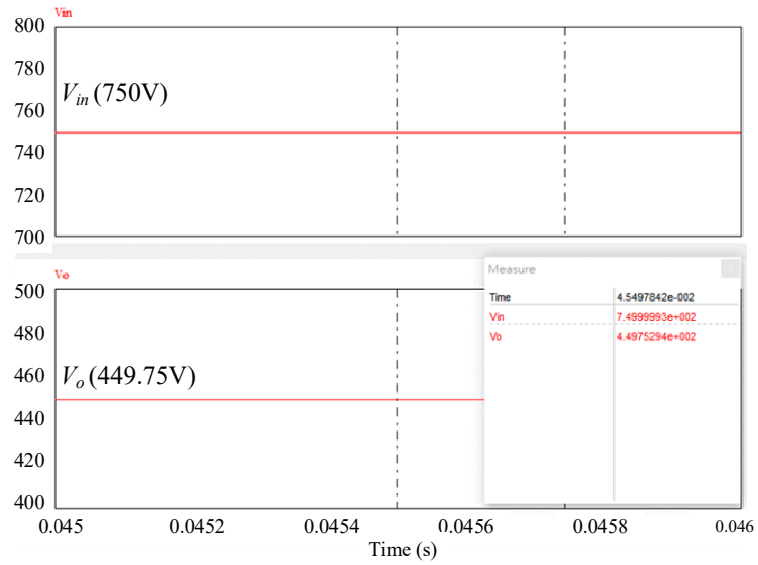


Figure 13. Input and output voltage waveforms of the inverter.

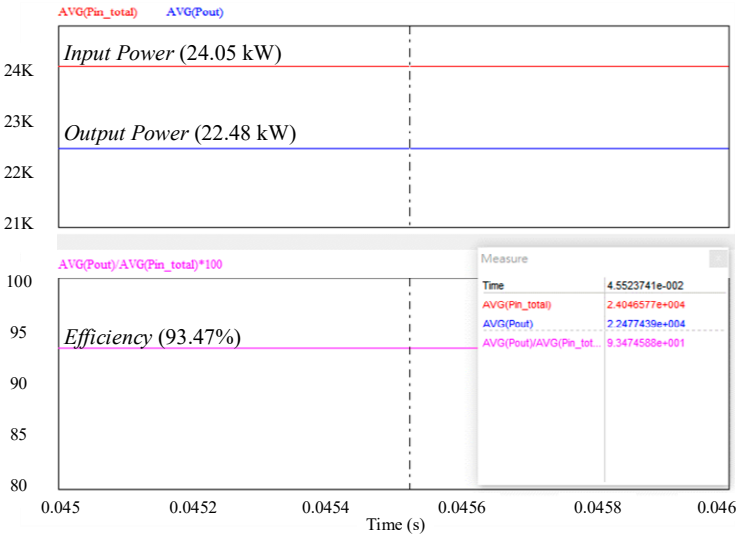


Figure 14. Input/output power and conversion efficiency of the proposed WPT system.



(**a**) (**b**)

Figure 15. Realized prototypes: (**a**) Tx coils; (**b**) Rx coils.



Figure 16. Photograph of the realized coil coupling.

Table 5. Measured results of the realized Tx/Rx coils.

Primary coils	L_{1a}	161.79 μH	Secondary coils		L_{2a}	158.69 μH
	L_{1b}	152.86 μH			L_{2b}	160.25 μH
	L_{1c}	158.83 μH			L_{2c}	164.07 μH
	M_{1b1a}	35.56 μH			M_{2b2a}	41.20 μH
	M_{1c1b}	39.52 μH			M_{2c2b}	41.25 μH
	M_{1a1c}	37.30 μH			M_{2a2c}	37.82 μH
Mutual inductances	M_{1a2a}	36.40 μH	M_{1b2a}	16.89 μH	M_{1c2a}	14.76 μH
	M_{1a2b}	13.84 μH	M_{1b2b}	36.56 μH	M_{1c2b}	14.81 μH
	M_{1a2c}	14.81 μH	M_{1b2c}	16.81 μH	M_{1c2c}	37.84 μH

5. Conclusions

This paper designed a three-phase 22 kW high-power WPT system through PSIM and CST STUDIO SUITE™ simulation. The WPT system used three-phase, sandwich-wound Tx/Rx coils to minimize the magnetic flux leakage effect and increase the PTE in order to transfer power effectively across the 170~250 mm air gap. A detailed equivalent circuit model has been derived for selecting the primary- and secondary-side coil inductors and capacitors. In this paper, the system simulation achieved a PTE of 93.47% at an operating frequency of 85 kHz with a 170 mm air gap between the coils. The results verify the feasibility of the simulation-assisted design. The developed coils can comply with a high-power and high-efficiency WPT system, as well as a size reduction. Based on the simulation-assisted design results, the realized prototype of the Tx/Rx coils was built; the tolerances of parameters are limited to 7~18% compared with the designed points. This paper shows promising results for the further implementation of the high-power WPT system.

Author Contributions: Conceptualization, Methodology, Supervision and Funding acquisition, C.-M.L.; Formal analysis and Writing—original draft, C.-H.W. and C.-M.L.; Writing—review and editing, C.-H.W. and T.M.; Data Collection, Z.-B.L. All authors have read and agreed to the published version of the manuscript.

Funding: This research was funded by the Ministry of Science and Technology, Taiwan, R.O.C., grant number MOST 110-2622-8-005-005-TE1, MOST-109-2622-E-005-009-CC2, MOST-107-2221-E-005-079-MY3, and MOST-110-3116-F-018-001.

Institutional Review Board Statement: Not applicable.

Informed Consent Statement: Not applicable.

Data Availability Statement: Not applicable.

Acknowledgments: The authors would like to acknowledge the support from Chien-Chih Lu, the former postdoctoral researcher at NCHU, Taichung, Taiwan.

Conflicts of Interest: The authors declare no conflict of interest.

References

1. Michaelides, E.E. Primary Energy Use and Environmental Effects of Electric Vehicles. *World Electr. Veh. J.* **2021**, *12*, 138. [CrossRef]
2. Garwa, N.; Niazi, K.R. Impact of EV on Integration with Grid System-A Review. In Proceedings of the International Conference on Power Systems, Perth, Australia, 10–12 October 2019; pp. 1–6.
3. IEA. Global EV Outlook 2021, IEA, Paris. Available online: https://www.iea.org/reports/global-ev-outlook-2021 (accessed on 28 October 2021).
4. Liu, D.; Zhang, T.; Wang, W.; Peng, X.; Liu, M.; Jia, H.; Su, S. Two-Stage Physical Economic Adjustable Capacity Evaluation Model of Electric Vehicles for Peak Shaving and Valley Filling Auxiliary Servicses. *Sustainability* **2021**, *13*, 8153. [CrossRef]
5. Brenna, M.; Foiadelli, F.; Leone, C. Electric Vehicles Charging Technology Review and Optimal Size Estimation. *J. Electr. Eng. Technol.* **2020**, *15*, 2539–2552. [CrossRef]
6. Lu, X.; Wang, P.; Niyato, D.; Kim, D.I.; Han, Z. Wireless charging technologies: Fundamentals, standards, and network applications. *IEEE Commun. Surv. Tutor.* **2016**, *18*, 1413–1452. [CrossRef]
7. Bosshard, R.; Kolar, J.W. Inductive power transfer for electric vehicle charging: Technical challenges and tradeoffs. *IEEE Power Electron. Mag.* **2016**, *3*, 22–30. [CrossRef]
8. Bojarski, M.; Asa, E.; Colak, K.; Czarkowski, D. A 25 kW industrial prototype wireless electric vehicle charger. In Proceedings of the IEEE Applied Power Electronics Conference Exposition, Long Beach, CA, USA, 20–24 March 2016; pp. 1756–1761.
9. Mi, C.; Buja, G.; Choi, S.Y.; Rim, C.T. Modern Advances in Wireless Power Transfer Systems for Roadway Powered Electric Vehicles. *IEEE Trans. Ind. Electron.* **2016**, *63*, 6533–6545. [CrossRef]
10. Matsumoto, H.; Shibako, Y.; Neba, Y. Contactless Power Transfer System for AGVs. *IEEE Trans. Ind. Electron.* **2018**, *65*, 251–260. [CrossRef]
11. Joseph, P.K.; Elangovan, D.; Sanjeevikumar, P. System Architecture, Design, and Optimization of a Flexible Wireless Charger for Renewable Energy-Powered Electric Bicycles. *IEEE Syst. J.* **2020**, *15*, 2696–2707. [CrossRef]
12. Feng, H.; Tavakoli, R.; Onar, O.C.; Pantic, Z. Advances in High-Power Wireless Charging Systems: Overview and Design Considerations. *IEEE Trans. Transp. Electrif.* **2020**, *6*, 886–919. [CrossRef]
13. Pathmanathan, M.; Nie, S.; Yakop, N.; Lehn, P.W. Field-Oriented Control of a Three-Phase Wireless Power Transfer System Transmitter. *IEEE Trans. Transp. Electrif.* **2019**, *5*, 1015–1026. [CrossRef]
14. Pries, J.; Galigekere, V.P.N.; Onar, O.C.; Su, G.-J. A 50-kW Three-Phase Wireless Power Transfer System Using Bipolar Windings and Series Resonant Networks for Rotating Magnetic Fields. *IEEE Trans. Power Electron.* **2019**, *35*, 4500–4517. [CrossRef]
15. Wang, C.; Zhu, C.; Wei, G.; Feng, J.; Jiang, J.; Lu, R. Design of Compact Three-Phase Receiver for Meander-Type Dynamic Wireless Power Transfer System. *IEEE Trans. Power Electron.* **2020**, *35*, 6854–6866. [CrossRef]
16. Mohammad, M.; Pries, J.L.; Onar, O.C.; Galigekere, V.P.; Su, G.-J.; Wilkins, J. Three-Phase LCC-LCC Compensated 50-kW Wireless Charging System with Non-Zero Interphase Coupling. In Proceedings of the 2021 IEEE Applied Power Electronics Conference and Exposition (APEC), Phoenix, AZ, USA, 14–17 June 2021; pp. 456–462. [CrossRef]
17. SAE J2954. Wireless Power Transfer for Light-Duty PlugIn/Electric Vehicles and Alignment Methodology. Available online: https://www.sae.org/standards/content/j2954_202010/ (accessed on 30 October 2021).
18. Mohamed, A.; Marim, A.A.; Mohammed, O. Magnetic Design Considerations of Bidirectional Inductive Wireless Power Transfer System for EV Applications. *IEEE Trans. Magn.* **2017**, *53*, 1–5. [CrossRef]
19. Safaee, A.; Woronowicz, K.; Maknouninejad, A. Reactive Power Compensation Scheme for an Imbalanced Three-Phase Series-Compensated Wireless Power Transfer System with a Star-Connected Load. In Proceedings of the IEEE Transportation Electrification Conference 316 and Expo, Long Beach, CA, USA, 13–15 June 2018; pp. 44–48.